Dynamics of coupled plasmon polariton wave packets excited at a subwavelength slit in optically thin metal films

Lei-Ming Wang,[1] Lingxiao Zhang,[2] Tamar Seideman,[2,]* and Hrvoje Petek[1,]*

[1]*Department of Physics and Astronomy, and Petersen Institute of NanoScience and Engineering, University of Pittsburgh, Pittsburgh, PA 15260*

[2]*Department of Chemistry, Northwestern University, 2145 Sheridan Road, Evanston, IL 60208*

*E-Mails: t-seideman@northwestern.edu, petek@pitt.edu

Abstract

We study by numerical simulations the excitation and propagation dynamics of coupled surface plasmon polariton (SPP) wave packets (WPs) in optically thin Ag films and a bulk Ag/vacuum interface under the illumination of a subwavelength slit by 400 nm continuous wave (cw) and femtosecond pulsed light. The generated surface fields include contributions from both SPPs and quasi-cylindrical waves, which dominate in different regimes. We explore aspects of the coupled SPP modes in Ag thin films, including symmetry, propagation and attenuation, and the variation of coupling with incident angle and film thickness. Simulations of the electromagnetic transients initiated with femtosecond pulses reveal new features of coupled SPP WP generation and propagation in thin Ag films. Our results show that, under pulsed excitation, the SPP modes in an Ag thin film break up into two distinct bound surface wave packets characterized by marked differences in symmetries, group velocities, attenuation lengths and dispersion properties. The nanometer spatial and femtosecond temporal scale excitation and propagation dynamics of the coupled SPP WPs are revealed in detail by movies recording the evolution of their transient field distributions.

I. INTRODUCTION

Surface plasmon polaritons (SPP) are guided electromagnetic modes of a metal/dielectric interface. These surface electromagnetic waves arise through the coupling of the incident electromagnetic radiation with the collective charge-density oscillations of the free electrons in a metal.[1, 2] Because of their strong field confinement and propagation at the local speed of light, SPP modes can both guide and localize electromagnetic fields at nanometer/femtosecond scales, and hence enable a variety of intriguing applications such as surface-enhanced spectroscopy,[3] biosensing,[4] nano-optics,[5] and coherent control.[6] A detailed understanding of the excitation and propagation of surface electromagnetic fields from the perspective of theoretical simulations validated by incisive ultrafast imaging experiments is essential for applications.[7, 8]

An SPP mode at a single metal/dielectric interface corresponds to a transverse magnetic (TM) wave. This mode propagates along the interface, with the field amplitude decaying evanescently into both media. Because of the mismatch in the propagation wave vectors, an incident radiation field in the dielectric cannot directly excite the SPP wave at an atomically smooth metal/dielectric interface. Rather, the SPP can be launched through several special excitation configurations or coupling structures, *e.g.,* prism,[9] grating,[10] four-wave mixing,[11] film discontinuity,[12] and so-called back-side illumination,[13, 14] that enable simultaneous energy and momentum conservation between the excitation and the scattered SPP fields. Once generated, the SPP wave propagates dispersively and dissipatively at the metal-dielectric interface according to its complex, frequency-dependent dielectric function.

For an optically thin metal film, the SPP modes of each interface couple to form two new eigenmodes representing the symmetric and antisymmetric linear combinations of the single-interface modes.[15] For an infinitely wide metal film embedded in a homogeneous dielectric

environment, these eigenmodes are conventionally named the symmetric (s_b) and antisymmetric (a_b) bound modes.[16] The s_b mode features a symmetric (asymmetric) distribution of its transverse (longitudinal) field components with respect to the plane of the film, and is characterized by weak field confinement within the metal slab and consequently a long propagation length. Thus, it is also called the long range SPP (LRSPP).[17] By contrast, the transverse and longitudinal components of the a_b mode exhibit the opposite behavior; because of its strong confinement within the metal, the a_b mode is strongly damped and is therefore termed the short range SPP (SRSPP). The LRSPP in thin metal films is of practical interest because its propagation distance can be one to two orders-of-magnitude longer than that of the corresponding single-interface SPP, though at the expense of reduced field confinement,[16, 18-20] while the strong confinement and large k-vector of SRSPP has potential applications for nanometer scale focusing of light at metallic tapers and tips.[21, 22]

The present investigation is motivated by our recent femtosecond (fs) time-resolved photoemission electron microscope (PEEM) imaging of the propagation of SPP fields at an Ag/vacuum interface of an 80 nm Ag film on Si substrate.[8] Experimentally, the SPP fields are excited by a femtosecond laser pulse illumination at a nanometer-scale slit in the Ag film. To unravel the information content of our measurements and understand their potential, we performed finite-difference time-domain (FDTD) simulations of the PEEM imaging. We found that the simulated patterns of the total surface fields exhibit unexpected spatial modulations, which could arise through coupling between the top- and bottom-surface SPP modes of the film.[8] Our simulations also showed that the shape of the total field modulation is further dependent on other factors such as the slit width, incident angle, and pulse duration. This motivated us to perform a systematic characterization of the scattered surface waves in a thin Ag film with

thickness comparable to the optical skin depth. In our study, we take into account conditions that are experimentally relevant, such as pulsed excitation and oblique incidence. So far, most of the theoretical analyses of coupled SPP modes in thin metal films have been carried out with an analytical approach solving for the momentum dependent eigenmodes for specific metal/dielectric structures[16, 23-25] More recently, numerical methods have also been developed, most of which, however, were also limited to solving for the eigenmodes.[26-33] Simulations of SPP-related systems with ultrashort pulse excitation have been few,[34, 35] and to the authors' knowledge none has been applied to the coupled SPP modes in thin metal films. Considering the femtosecond scale lifetimes of SPPs, a detailed understanding of the dynamics of the coupled SPP excitation and propagation is essential for applications in, *e.g.*, coherent control of ultrafast plamonics.[6, 12, 36, 37] To explore in a uniform fashion both the excitation and the subsequent propagation dynamics of the SPP waves, which can be directly compared with experiments, it is useful to apply a method which is capable of: (*i*) incorporating the exact excitation geometry; (*ii*) separating the scattered surface waves from the incident field; and (*iii*) tracking the field distributions in time. The goal is to characterize total surface fields that can be directly compared with nonperturbative methods, such as PEEM imaging, on similar nanometer spatial and femtosecond temporal scales.

With these goals in mind, we develop a numerical simulation within the FDTD framework,[38] which is capable of calculating the fields upon injecting obliquely incident plane wave into arbitrary dispersive layered media. We apply the method to explore scattering at a nanometer slit in a thin silver film. Both cw and short pulse excitations are considered. The results show that the slit scattering generates interfacial fields consisting of not only the SPP modes, but also a quasi-cylindrical wave (QCW).[39-42] The two modes are excited at a nanometer

4

asperity with different amplitudes, and decay with different dependences on the distance from the source. The QCW has both far- and near-field contributions; its transverse field components (E_y & H_z) at the surface (near-field) are phase shifted with respect to the corresponding radiating wave in the far field.[43] The far- and near-field components of QCW also have been refered to as "ray-optics" (RO) and "Norton wave" (NW), respectively.[44] We only consider the near-field component, whose role in nanoplasmonic phenomena has been a subject of significant debate and controversy.[41, 42, 45-47] The relative contributions of the QCW and SPP to the total field amplitudes at different spatial regions relevant to the PEEM measurement are evaluated. The relative excitation efficiencies of the coupled SPP modes with respect to the incident angles, and the dependence of the dispersion relation on the film thickness are systematically investigated. Simulations with femtosecond pulse excitations reveal new interesting phenomena regarding the ultrafast dynamics of the coupled SPP wave packets, which can guide future space- and time-resolved experiments on surface-confined electromagnetic fields at metal-dielectric interfaces.

II. NUMERICAL METHOD

The simulations are carried out in two dimensions using a self-developed fully vectorial 2D-FDTD simulation code. The method is similar to that used in our previous studies on the imaging of ultrafast SPP dynamics by PEEM.[8, 48, 49] Figure 1 shows a schematic illustration of the simulation domain. Briefly, a thin silver film of thickness h, with a slit of width d serving as the scattering structure, is placed in the x-z plane. The simulations are performed in the cross sectional plane (x-y) formed by the incident wave vector and the normal direction of the film surface, $i.e.$, the optical plane for the light-matter interaction. A p-polarized (TM) plane wave incident at an angle Θ with respect to the surface normal is introduced into the simulation domain through a total-field/scattered-field (TF/SF) approach.[38] As shown in Fig. 1, the total

field (TF) comprises of both the incident and the scattered contributions, and scattered field (SF) regions are separated by the TF/SF boundary (dashed rectangle). At each FDTD time step, field corrections are applied to all the nodes adjacent to the boundary by either adding or subtracting the incident field values such that the fields propagating inside the box represent the TF, while those outside the box are purely the SF. The incident field along the boundary is obtained numerically via an auxiliary 1D FDTD simulation of modified 1D Maxwell's equations[49-52] that describe rigorously the 1D plane wave propagation through layered media ("vacuum-Ag-vacuum" in the current case) with an effective phase velocity that matches the projection of the obliquely incident 2D wave phase velocity onto the y axis. This means that the multiple reflection and transmission at the upper and lower interfaces of the film are included in the incident fields, so that fields emerging in the SF region are purely due to scattering effects caused by the slit structure. Both the 1D and 2D FDTD grids are terminated with the convolutional perfectly matched layer (CPML, the brown shaded area in Fig. 1) absorbing boundary condition, which effectively absorbs both propagating and evanescent waves impinging upon it from all directions.[53, 54]

The simulations are performed with a 400 nm incident wavelength (center wavelength in the case of pulsed excitation), as is commonly used in the two-photon photoemission measurements of surface plasmon dynamics.[8, 12] In this wavelength regime, the dielectric function of Ag is reasonably well described by the Drude model with the relative permittivity expressed as

$$\varepsilon_{Ag}(\omega) = \varepsilon_{\infty} - \frac{\omega_d^2}{\omega^2 + i\gamma_d \omega} \tag{1}$$

The values of the coefficients in Eq. (1) are obtained from a fit of the experimental dielectric constants of bulk Ag by Johnson and Christy[55] in the spectral range of 330 to 500 nm, which gives $\varepsilon_\infty = 7.0246$, $\omega_d = 1.5713 \times 10^{16}$ rad/s, and $\gamma_d = 1.4003 \times 10^{14}$ rad/s. This model for the dielectric function, however, does not include the contribution from Landau damping, that is expected in quantum confined structures.[56, 57] The auxiliary differential equation (ADE) approach is employed to model the material dispersion, in which ADEs of the polarization currents accounting for the single-pole Drude response are solved along with those of the electric fields.[38] Compared with the uniaxial perfectly matched layers (UPML) method used in our previous simulations,[8, 48, 49] the ADE method combined with CPML is more efficient for systematically treating general dispersive media with multi-poles. Due to the discretized nature of the FDTD grids, the exact position of the material interface can be ambiguous. In the current study, the Ag-vacuum interfaces are all aligned with the electric field nodes, and an averaged dielectric permittivity is used for updating the electric fields at the interfaces. Such averaging has been shown to improve the convergence.[49]

For cw simulations the excitation source is a magnetic field of the temporal form $H(t) = H_0 \sin(\omega_0 t)$, where $\omega_0 = 2\pi c/\lambda_0$ and $\lambda_0 = 400$ nm. The amplitude of the H field is set to $H_0 = 1$ (A/m). Paired with this magnetic field is the incident electric field with the field amplitude $E_0 = H_0 Z_0$ (V/m), where $Z_0 = \sqrt{\mu_0/\varepsilon_0}$ is the impedance of free space. To avoid high frequency components in the leading wave front, which could cause leakage through the TF/SF boundary, the incident field is gradually ramped to its maximum amplitude using a Gaussian rising envelope function. The pulsed excitation is described by a Gaussian pulse

$$H(t) = H_0 \exp[-\frac{(t-t_0)^2}{\tau^2}]\sin(\omega_0 t),$$ where τ is related to the full-width at half-maximum (*FWHM*)

of the field envelope of the pulse as $\tau = FWHM / 2\sqrt{\ln 2}$, and the pulse center is set to $t_0 = 3\tau$ in all calculations. Unless otherwise stated, the simulations are done for a region of 13.2 x 1.6 μm², with a spatial step (grid size) of $\Delta x = \Delta y = 2$ nm. A Courant number $S_c = c\Delta t / \Delta x = 0.4$ is used, giving a time step of $\Delta t \approx 2.6685$ as. Separate tests have been performed to ensure numerical convergence with the chosen parameters.

III. RESULTS AND DISCUSSIONS

A. Single Ag-vacuum interface

We begin this section by describing the light scattering at a subwavelength object at a single Ag-vacuum interface, which provides a reference for the discussion of the coupled SPP modes in thin films. For this purpose, the Ag film in Fig. 1 is replaced by a semi-infinite Ag slab, the surface of which is at y = 0. A groove of 200 nm wide and 100 nm deep on the surface serves as the subwavelength scatterer to couple the external field into the SPP mode. Because our focus here is on the SF, a relatively small TF box of 600 x 600 nm is used. A 400 nm cw plane wave is incident at $\Theta = 65^\circ$. The coupling structure, excitation geometry, and other parameters in the simulations are typical for our PEEM experimental configuration.[8, 12, 48, 58] Figure 2(a) displays a snapshot of the steady state magnetic field distribution ($|H_z|$), taken at $t = 106.74$ fs. The result clearly shows that the scattered waves are comprised of two components: a guided bound mode propagating along the interface with the characteristics of a SPP wave, and a radiating mode, which is the QCW. It has been shown that the amplitude profile of the far-field component of QCW has an essentially cylindrical wave front and $r^{-1/2}$ decay from the source [Fig. 2(a)], while its near-field component is primarily confined at the surface and has an asymptotic $x^{-3/2}$ dacay.[43, 44] The near-field component of the QCW is overwhelmed by SPP within the range simulated in Fig. 2; it becomes dominant and can be characterized in a simulation for longer propagation

distance than the SPP decay length, as will be discussed below. The wavelengths of the SPP and QCW waves are measured to be 348 and 400 nm,[59] respectively, consistent with the expected wavelengths (the analytical value of SPP is 348.25 nm). Within the simulation range, the surface field is dominated by the SPP, whereas interference between SPP and QCW is most clearly visible in Fig. 2(a) in vacuum at about 400 nm below the interface.

Other features directly revealed in Fig. 2(a) are the different intensity of the forward ($+x$) and backward-propagating ($-x$) SPP excited at the slit, and the asymmetric angular distribution of the QCW with respect to the groove center, both of which are clear consequences of the oblique incidence geometry. The difference between the forward and backward scattered SPP waves for oblique incidence has been observed in the PEEM imaging experiments.[8] Henceforth, we only focus on the forward-propagating SPPs, i.e., $x > 0$. Note that we define the center of the slit as the origin ($x = 0$) throughout this work, and analyze the field only in the SF region (*i.e.*, $x > 0.3$ µm) in the following discussion.

In Fig. 2(b), the magnetic field profile at the Ag surface is plotted as a function of the x coordinate. The field amplitude exhibits a clear decay as the SPP propagates away from the origin. An exponential fit to its envelope (dashed line) gives an attenuation constant of 2.32 x 10^5 m^{-1} (*i.e.*, a propagation distance of 4.31 µm), which matches well the analytical value calculated from the dispersion function of the imaginary part of the wave vector k_{spp} for the Ag/vacuum interface (Table I). Note that the first two oscillation cycles deviate from the exponential trend, which is probably due to an appreciable contribution from the QCW near the origin,[39, 42] and thus are omitted from the fit.

We now examine the near-field surface component of the QCW. Because the SPP and QCW have different attenuation rates along the propagation direction (exponential vs. power law), we expect that beyond a certain distance the QCW will dominate the scattered surface field.[44, 60] To qualitatively evaluate the contribution of the QCW to the total surface field at different distances, we performed an additional simulation on a larger horizontal scale of 60 μm. Figure 3 presents the envelope (peak maxima) of the calculated H_z field at the interface as a function of propagation length in the x-direction. The simulation shows that, for the considered system, the SPP dominates the surface field within ~30 μm from the origin, *i.e.* much longer than the characteristic attenuation length. The amplitude of the two components becomes comparable for 30<x<40 μm, where strong interference structures with a period of ~2.7 μm appear. Beyond that, the field amplitude deviates from the exponential decay of SPP and approaches the power law characteristic of a QCW. For comparison, the total surface field was also calculated using the analytical model by Nikitin *et al*[44] as the sum of SPP and QCW (i.e. the NW in Ref.44) contributions. As shown in Fig. 3, despite small differences in the relative amplitudes between the model calculation (assuming infinitesimal slit width and asymptotic power law decay of QCW) and the numerical result, both methods describe the overall profile of the total scattered surface field. The SPP and QCW contributions to the total surface field can be better distinguished in a simulation of pulsed excitation. The movie S1 (supplemental material[61]) shows the temporal evolution of H_z field profile (and its Fourier spectrum) at the interface, calculated on a same system as in Fig. 3 but for excitation with a ~10fs pulse, which clearly reveals the separation and evolution of the SPP and the QCW WPs as well as their interference. Although beyond 40 μm the QCW dominates the surface field, its relative strength is <10^{-3} compared with the incident field. Based on this simulation, the relative contribution of the QCW to the total

surface field relevant to the PEEM experiments ($x < 15$ μm, 400 nm excitation) is negligible, except for a region of $< 2\lambda_0$ from the groove.

The transverse confinement of the SPP field is illustrated in Fig. 2(c), in which the field distribution at a fixed x position [marked by a double arrow in Fig. 2(a)] is plotted as a function of the y coordinate into each medium. The circles show the FDTD results, and the red and blue curves show simple exponential fits to the FDTD data. The decay constants obtained for fields within the two media are listed in Table I and compared to the corresponding analytical values. The decay constant in the metal (k_{y1} in Table I) gives a skin depth of 27.3 nm for Ag at 400 nm.

B. Coupled SPP modes in thin films. CW excitation

In this section, we focus on the case of a plane wave scattering at a nanometer slit in a thin Ag film. We first consider an Ag film of 20 nm thickness with a 200 nm wide slit, excited by a p-polarized cw plane wave incident in the surface normal direction ($\Theta=0$ in Fig. 1). Figure 4(a) presents the normalized electric and magnetic field distributions at steady state (133.43 fs). In contrast to scattering at a single interface, three components can be identified within the scattered wave region. The QCW is similar to the single interface case, but is scattered both above and below the Ag film, and each field component of QCW in Fig. 4(a) has a symmetric distribution with respect to the center of the slit ($x = 0$), reminiscent of the dipole emission from a sub-λ source.[43] As for the single interface, the QCW makes a noticeable contribution to the total surface field only under special circumstances, as will be discussed below.

Besides the QCW contributions, the surface fields in Fig. 4(a) are dominated by two bound modes: a strongly confined and rapidly decaying wave near the origin (short range, $x \sim 0 - 2$ μm), and a weakly bounded but slowly decaying wave that is clearly discernable only at large

distances (long range, $x>6$ μm). These are the characteristics of the a_b and s_b coupled SPP modes in thin metal films as described in the introduction. To confirm their identity and characterize them in more detail, we first determine their wavelengths to be 208 and 394 nm, in agreement with the analytical values of 208.3 nm and 393.3 nm obtained by solving the corresponding transcendental dispersion relations.[16] Furthermore, the symmetries of the two modes with respect to the central plane of the film ($y=0$) can be established from the field distributions, as displayed in Fig. 5. We find that for the a_b mode (SRSPP) the longitudinal field components (E_x) at the two interfaces are in-phase, $i.e.$, symmetric across the film, whereas the transverse components (E_y and H_z) are out-of-phase and anti-symmetric, resulting in a nodal structure passing through the metal slab. By contrast, the s_b mode (LRSPP; insets of Fig. 5) displays an antisymmetric (symmetric) distribution of its longitudinal (transverse) field components with respect to the film plane. The symmetry of the H_z field is further illustrated in the enlarged views of the field distributions at two regions in the color plot insets in Fig. 5(c) to confirm that the two surface waves are the a_b and s_b coupled SPP modes. The symmetry properties of the a_b mode distribution are associated with longitudinal electron oscillation with a symmetric electron distribution over h, whereas the s_b mode is associated with a normal electron oscillation with an antisymmetric charge distribution over h.[15, 62]

As can be seen in Fig. 4(a), despite the interference among the three scattered surface wave components, different regions are dominated by specific modes, as in the case of the single interface. For instance, near the origin ($x<2$ μm) the field is dominated by the a_b mode. Its propagation length is estimated to be 0.52 μm by an exponential fit to the H_z field profile shown in Fig. 5(c) in the range of $x = 0.3$ to 1.9 μm. The substantially shorter propagation length compared with the SPP of a single Ag-vacuum interface clearly establishes the SRSPP nature of

the a_b mode. In contrast to the a_b mode, the s_b mode is much weaker under normal incidence excitation. Thus, the considerable interference with the QCW prevents the evaluation of the s_b decay profile along the surface through an exponential fit. Note that the wavelengths of LRSPP (394 nm) and QCW (400 nm) are very close for a 20 nm thin film, so that the interference between the two fields takes on a different character than for the thick slab case in Fig. 3. In order to estimate the propagation length of the s_b mode, we perform an additional simulation for a longer grid of 60 μm at 65° incidence, for which the excitation efficiency of LRSPP is larger than for the normal incidence. As shown in Fig. 6, the calculated H_z field envelope at the lower interface of the film follows a clear exponential decay trend only for $x>30$ μm, which we attribute to LRSPP. In the intermediate region ($x = 2$ to 30 μm) the interference among SRSPP, LRSPP and QCW results in complicated field profile [see also Fig.4(b)]. This is in contrast to the case of single Ag-vacuum interface where the SPP component dominates over the region of $x<15$ μm, because for the thin film LRSPP has a relatively small amplitude but a long attenuation length. From the exponential decay profile, an attenuation length of 86 μm is estimated for the s_b mode of the 20 nm Ag film upon 400 nm excitation, consistent with its LRSPP character.

C. Incident angle-dependent relative excitation efficiency

As already noted, under normal incidence, the excitation efficiency of the s_b mode is low compared with the a_b mode [Fig. 4(a) and Fig. 5]. This is because the incident field has only E_x and H_z components; without the E_y component, the field can drive the normal charge density oscillation only through diffraction at the slit, and therefore coupling to the predominantly transverse s_b mode is weak. We reason that introducing the E_y component into the incident field by oblique incidence should enhance the relative excitation efficiency of the s_b LRSPP. Indeed, an end-fire coupling scheme has been suggested, in which the incident beam is focused onto the

end facet of the film such that it is well matched with the field profile of the s_b mode.[16] Such arrangement corresponds to a 90° incidence angle, which cannot be realized in the current simulation. Instead, we investigated the relative excitation efficiencies of the coupled SPP modes in the $0\sim75^o$ incidence angle range.

Figure 4(b) presents the simulation results for 65° incidence upon a 20 nm thick Ag film, with all other parameters kept as in Fig. 4(a). Comparison of Figs. 4(a) and 4(b) shows that oblique incidence enhances coupling into the s_b mode relative to the a_b mode. Specifically, under normal incidence, the E_x component of the s_b mode is hardly seen on the color scale, implying that its intensity is below 10^{-3} with respect to the incident electric field [Fig. 4(a)]. On the same intensity scale, however, a weakly confined surface wave is clearly seen with the 65° oblique incidence [Fig. 4(b)]. Similarly, in contrast to the normal excitation, the intensities of the transverse field components E_y and H_z are dominant over that of the QCW. Also, Fig. 4(b) reveals that with comparable field intensities, the a_b and s_b modes (for the major components E_y and H_z) exhibit strong interference in the short-range region ($0<x<2$ μm).

Whereas the scattered fields display complex spatially varying interference patterns, a Fourier transform analysis of the field profiles with respect to the propagation distance along the interface gives a simpler description of the field components in terms of their spatial frequencies, amplitudes, and lineshapes. Figure 7 displays a series of Fourier spectra of the H_z profiles along the lower interface of a 10 nm thick Ag film in vacuum for incidence angles ranging from 0 to 75°. Two major Fourier components appear at 0.016 and 0.052 nm^{-1}, corresponding to the real parts of the wave vectors (denoted as β_R) of the s_b and a_b coupled SPP modes (the analytical values are 0.0158 and 0.0524 nm^{-1}). As shown in Fig. 7, the peak positions of the two coupled modes do not vary with the incident angle, because their dispersion relations are solely

determined by the material properties and the slab thickness. The Fourier amplitudes of the two modes, however, vary strongly with the incident angle. Particularly, the relative amplitude ascribed to the s_b mode increases significantly from 0 to 75° incidence (Fig. 7 inset), confirming effective excitation of the LRSPP for large oblique incidence angles. We note that for a 10 nm thick Ag film, the wavelengths of the QCW and the LRSPP (s_b) are nearly the same (400 vs. 398 nm), and therefore are not resolved in the Fourier spectra in Fig.7. Hence the peak corresponding to the s_b mode at 0.016 nm^{-1} also contains the contribution from the QCW component, which could be appreciable particularly for normal incidence, where the excitation of LRSPP is inefficient. Indeed, a close examination reveals that the E_x component at the surface for a 0° incidence angle and a 10 nm film is dominated by the QCW over the x=2 to 12.5 μm range (not shown). This is evident because the QCW has different symmetry with respect to the film plane and damping characteristics compared with the LRSPP. The QCW contribution is smaller, however, for the transverse components E_y and H_z, or for thicker (e.g., 20 nm) films at all incidence angles. Nevertheless, the relative variation of the Fourier amplitudes reflects the excitation efficiency of the coupled SPP modes with the incident angle.

D. Film thickness dependent coupled mode dispersion relations

The coupling between the SPP modes at each interface depends on the film thickness, and this, in turn, affects the coupled mode dispersion relations. Figure 4(c) shows the steady state field distributions for a 10 nm Ag film and a 65° incidence angle excitation. Compared with the 20 nm film in Fig. 4(b), one can see that the properties of the a_b and s_b modes diverge with decreasing film thickness. Specifically, as the film thickness decreases from 20 nm to 10 nm, the a_b mode wavelength decreases from 208 to 120 nm (or equivalently the propagation constant β_R increases from 0.03 to 0.053 nm^{-1}), and its attenuation length decreases from 0.52 to 0.26 μm.

15

With decreasing film thickness, the a_b mode becomes dominated by the longitudinal field (E_x) and is confined more strongly within the metal, because an antisymmetric transverse field cannot exist in vacuum. The increased confinement within the metal film leads to a smaller propagation distance. By contrast, comparing the same films, the wavelength of the s_b mode, which is dominated by the transverse field component, increases from 394 to 398 nm (β_R decreases from 0.0159 to 0.0157 nm^{-1}), approaching the free space value of $\lambda_0 = 400$ nm. At 10 nm, the s_b mode is only weakly confined to the metal and penetrates deeply into the vacuum, acquiring the appearance of a homogenous plane wave. For a vanishingly thin film, the s_b mode becomes the fundamental TEM mode of the dielectric medium, for which both the confinement and attenuation vanish.

The dependence of the propagation constant of the coupled SPP modes on the film thickness is illustrated in Fig. 8, which displays the Fourier spectra of the H_z field profiles at the lower interface of the film, from simulations for Ag films with varying thickness h. Again, two major components corresponding to the a_b and s_b modes are revealed. In addition, for thick films (e.g. > 50 nm), the QCW component is also discernable at 0.0157 nm^{-1} as a shoulder in the left wing of the s_b peak in the Fourier spectra [vertical dotted line in Fig. 8(a)]. Both the a_b and s_b modes vary systematically, with the a_b mode having a stronger dependence of the wave vector β_R on the film thickness, consistent with previous analytical results.[15, 16] The variation of the imaginary part of the coupled SPP wave vector (attenuation constant, β_I) is not evaluated, because for films thicker than 20 nm, the a_b and s_b modes strongly overlap. The propagation constants (β_R) from the Fourier analysis normalized to the free space wave vector of the incident field are plotted with respect to the film thickness and compared with the analytical values in Fig. 8(b). The results show that, with 400 nm excitation, the a_b and s_b modes become indistinguishable and converge

to the uncoupled single-interface SPP limit when the Ag film thickness exceeds 120 nm, corresponding to 4 times of the skin depth (27.3 nm).

E. Coupled SPP wave packets in thin films. Pulsed excitation

As we have shown, the two coupled SPP modes of thin Ag films have different propagation constants and predominant component of the field polarization. Differences in their nanometer spatial and femtosecond temporal scale light-matter interactions should be most clearly expressed in simulations for pulsed excitation, which we describe in this section.

Figure 9 presents snapshots of the scattered electric field distributions in a 20 nm thick Ag film at different times after the interaction of a ~10 fs intensity (14.14 fs field amplitude) width laser pulse incident at $\Theta=45^{\circ}$ with a 200 nm width slit. As expected, two distinct SPP WPs with different confinement and propagation properties are excited (Fig. 9). The symmetric and anti-symmetric field distributions identify the leading and the trailing WP as the s_b and a_b modes. Their dramatically different group velocities are responsible for their increasing separation with time in the snapshots of Fig. 9. At $t = 35.36$ fs, which is just after the external field has completed interacting with the slit, the QCW and the s_b WPs are fully formed and are superposed, whereas the trailing a_b WP is still only partly excited. The interference between the two modes, as well as the QCW, can be observed most prominently in the region about 1 μm from the source [Fig. 9 (a)]. At $t = 50.03$ fs, the incident field has completely transited, and the two WPs are fully launched and spatially separated due to their different group velocities [Fig.9 (b)]. The separation grows with time, and at $t = 65.38$ fs the s_b WP starts to exit the simulation domain [Fig. 9 (c)]. A snapshot of the transverse electric field, E_y, at the same instance is displayed in Fig. 9 (d) for comparison with that of the E_x. It shows that for a 20 nm film the s_b WP amplitude is dominated by the transverse field, in line with the corresponding s_b coupled mode in the cw-case. As a result,

17

the E_y field components of the two WPs are not yet completely separated in space; the interference between them is discernible in the WP tails at x ~ 3 μm where their amplitudes are comparable [Fig. 9 (d)]. To better view the time domain details of excitation and propagation dynamics of the coupled SPP WPs, a series of snapshots are recorded during the simulation, with a temporal step of ~ 0.667 fs (one-half of the time period of the field oscillation), and combined into a movie for each field component (presented in the supplemental documents[63]).

Another interesting difference between the coupled SPP WPs are their decay rates, which can be readily assessed from the relative amplitude drop of the E_x field from $t = 50.03$ to 65.36 fs in Fig. 9. The faster decay of the a_b WP occurs because it is more strongly confined to the lossy metal film, resulting in a larger dissipation. Also a consequence of strong confinement to the metal is the larger dispersion of the a_b WP as compared with the s_b WP. As seen in Fig. 9, as it propagates away from the origin, the spatial profile of the a_b WP deviates from a Gaussian shape, such that the leading front of the WP has a longer wavelength and lower intensity than its tail. The WP reshaping is a consequence of dispersion of both the propagation velocity and the damping. By contrast, the dispersion of the s_b WP is nearly indiscernible, consistent with the dispersion relations for the a_b and s_b coupled SPP modes in metal films.[15]

A quantitative analysis of the propagation and attenuation of the s_b and a_b WPs is presented in Fig. 10. By plotting the peak maxima as the function of time for the s_b and a_b WPs in Fig. 10 (a) and (c), their group velocities are determined to be 0.90c and 0.13c (c is the vacuum speed of light), respectively. Similarly, in Fig. 10 (b) and (d), the peak heights of the two modes are plotted as functions of its x coordinate, from which the attenuation lengths for the s_b and a_b WPs are estimated to be 73 and 0.5 μm. Again, the attenuation constant of the s_b WP is obtained from a separate calculation for a longer horizontal scale of 60 μm [Fig. 10 (b)]. Compared with the

results from the cw-calculations (86 μm and 0.52 μm for the s_b and a_b mode, respectively), the difference in the attenuation lengths for the s_b component is likely due to the different ways in which the contamination by the QCW and dispersion affect the amplitudes.

The variations of the s_b and a_b coupled WPs with incident angles and film thicknesses are fully analogous to those of the corresponding SPP modes in the cw-case. For instance, large angle incidence enhances the coupling of the s_b WP, while suppressing that of the a_b WP. The oblique incidence also causes asymmetry in the relative amplitudes of the same WP on two sides of the slit. As the film thickness increases, the propagation velocities and attenuation distances of the coupled SPP WPs converge. As an example, for a 30 nm thick Ag film, the group velocities of the s_b and a_b WPs are calculated to be $0.83c$ and $0.21c$, whereas for the 10 nm film they are $0.97c$ and $0.06c$. For film thickness exceeding 50 nm, it is difficult to distinguish the two WPs within the simulation range of 12.5 μm.

Pulsed excitation of the coupled SPP modes in a thin metal film offers a novel way of coupling a light pulse into two guided surface WPs with very different properties. Because they propagate at different group velocities, the interference of the s_b and a_b WPs can be studied by interferometric control over identical pump-probe pulse delay. Our preliminary simulations reveal novel interference effects in collisions of the s_b and a_b WPs of pump and probe pulses. Further experimental and theoretical investigations of the coupled SPP WPs in thin metal films as a function of, *e.g.*, the pump-probe delay and the pulse duration, will illuminate the coherent control of the surface fields at the nano-meter spatial and femtosecond temporal scales.

IV. CONCLUSIONS

We introduced a time-domain numerical approach to explore the coupling of obliquely incident fields into the plasmonic and photonic modes of metal/vacuum interfaces of solid and thin films. While our main interest is in describing new physical phenomena related with the phase and amplitude structure of modes excited by ultrashort pulsed excitation fields, we also investigated the case of cw-excitation to validate our approach through comparison with well established analytical theory. The method was applied to the excitation and propagation of surface plasmon polariton waves excited with 400 nm light at a bulk Ag surface and in thin Ag films. For both cases, the simulation shows that light scattering at a subwavelength structure generates not only SPP (and coupled SPP) waves, but also a quasi-cylindrical wave (QCW). For silver in the violet-UV range the SPP fields dominate at the interface, but the QCW contribution can be discerned at different distances from the coupling structure along the propagation direction, because of the different attenuation properties of the two modes. The dependence of the SPP and QCW field strengths on the in-plane and out-of-plane distances implies that the importance of each component will depend on the particular experiment. For example, PEEM experiments do not perturb the near-field distributions and are predominantly sensitive to the SPP fields, whereas near-field scanning probe experiments are likely to scatter both fields, and therefore probe a complex, distance-dependent convolution.

The two bound coupled s_b and a_b SPP modes propagate as predominantly transverse and longitudinal fields in thin films. Simulations conducted with different incidence geometries show that the coupling efficiency of the LRSPP (s_b mode), upon the scattering at the 200 nm slit, can be significantly enhanced at large oblique incidence angles. The simulations exhibit the dependence of the dispersions of the s_b and a_b coupled modes on the film thickness in agreement with the analytical results. Our results indicate that the coupling between the two SPPs supported

by the lower and upper surface of an Ag film, under 400 nm excitation wavelength, becomes negligible when the film thickness is larger than 120 nm.

Simulations with femtosecond pulsed excitation revealed new physical phenomena. We demonstrated that upon illumination by a ~10 fs laser pulse, the two coupled SPP modes of a thin film evolve into two bound surface wave packets distinguished by marked differences in their symmetry, propagation, and attenuation properties. The leading symmetric WP with predominantly transverse character (s_b WP) travels at a group velocity approaching that of light in vacuum. It is loosely bound, and exhibits a small attenuation and dispersion along its propagation. By contrast, the trailing asymmetric WP with predominantly longitudinal character (a_b WP) is strongly confined to the metal film. It propagates slower, decays at a faster rate, and displays stronger dispersion. The dependence of the s_b and a_b coupled WPs on the incident angle of the excitation field and the film thickness is the same as the component cw s_b and a_b coupled SPP modes that comprise the WPs. The dynamics of the coupled SPP WPs in the thin Ag film are revealed by movies of the field distributions evolving in space and time. The knowledge of the coupled SPP WPs dynamics in thin metal films is a prerequisite for designing coherent surface electromagnetic field manipulation experiments at the nanometer/femtosecond scale.

ACKNOWLEDGMENTS

the W. M. Keck Foundation grant on "Femtosecond time-resolved microscopy of single molecule machines"

Table I. Comparison of FDTD and analytically calculated propagation and decay constants for 400 nm light excitation of the Ag-vacuum interface SPP.

	FDTD	Anal.
$\text{Re}[k_{\text{spp}}]$ (10^7 m^{-1})	1.81	1.80
$\text{Im}[k_{\text{spp}}]$ (10^5 m^{-1})	2.32	2.33
k_{y1} (y>0, Ag) (10^7 m^{-1})	3.67	3.67
k_{y2} (y<0, Vacuum) (10^6 m^{-1})	8.97	8.88

Figure Captions

Fig. 1. A schematic representation of the 2D FDTD simulation. See the text for detailed description. The dimensions are not to scale.

Fig. 2. (a) The modulus of the calculated magnetic field distribution for 65° obliquely incident plane wave scattering at a 200 nm wide, 100 nm deep groove at an Ag/vacuum interface located at $y = 0$. The coordinates of the groove structure are $x = $ [-0.1, 0.1] and $y = $ [0, 0.1] μm. The rectangular box enclosing $x = $ [-0.3, 0.3] and $y = $ [-0.3, 0.3] μm is the TF/SF boundary. The field modulus is normalized to the incident magnetic field amplitude H_0, and a log color scale is used here and in all the field distribution figures below. (b) Magnetic field distribution at the Ag-vacuum interface vs x (determined at $y = $ -1 nm). The red curve is an exponential fit to the envelope of the field oscillations. (c) The transverse profile of the magnetic field intensity as a function of y at the x position marked with a double arrow in (a). The circles are the FDTD results, and the red and blue curves are exponential fits to the FDTD data.

Fig.3. Calculated H_z field envelope (at y=-1 nm) as a function of x for scattering at a nanoscale groove in a single Ag-vacuum interface. The red curve is an exponential fit of the SPP damping during the propagation along the interface. Beyond ~ 40 μm the surface field is dominated by a QCW, which has a power-law decay. The oscillations in the intermediate region with a period of 2.7 μm correspond to interference between SPP and QCW fields, which propagate with different k-vectors. The green curve is calculated using the model presented in Ref. 44 (multiplied by a normalization constant of 4).

Fig. 4. (a) Field amplitude modulus distributions of (i) E_x, (ii) E_y, and (iii) H_z for a normally incident plane wave scattering at a 200 nm wide slit cut through a 20 nm thick Ag film, showing

the generation of the a_b and s_b coupled SPP, as well as the QCW modes, and their interferences. The central plane of the Ag film is set at $y = 0$. The left and right edges of the slit are aligned at $x = -0.1$ and $x = 0.1$ μm, respectively. The amplitudes of the electric (E_x, E_y) and magnetic (H_z) fields are normalized to those of the corresponding incident fields E_0 and H_0. (b). As in (a) for 65° incidence angle. (c) As in (b) for a 10 nm thick film.

Fig. 5. Field profile at the upper (blue) and lower (red) interfaces of the 20 nm Ag film for (a) E_x, (b) E_y, and (c) H_z field components as shown in Fig. 4 (a). The insets at the upper-right of each frame show an expanded view of the corresponding field profile for x=8 to 12 μm. The 2D color plot insets in (c) are expanded views of the H_z field distributions of the a_b and s_b coupled SPP modes (displayed with different color scales to enhance the contrast), showing their different symmetry with respect to the film plane.

Fig.6. A plot of the calculated H_z field envelope (maxima) at the lower interface of a 20 nm Ag film as a function of propagation distance x for 65° off-normal illumination, showing the competition and interference among the generated QCW, SRSPP and LRSPP modes at different propagation distances. The red line is an exponential fit of the predominantly LRSPP component corresponding to an attenuation length of 86 μm.

Fig. 7. Fourier transform of the calculated H_z field profile at the lower interface of a 10 nm thick Ag film for different incidence angles. The inset shows the amplitudes of the two Fourier components as functions of the incidence angle. The s_b amplitude includes a contribution from the QCW, which has essentially the same propagation constants.

Fig. 8. (a) Fourier transform of the calculated H_z field profile at the lower interface of the Ag film with different thickness indicated at the left side under 65° off-normal illumination. The red

and blue dashed lines are to guide the eye. The QCW contribution is responsible for the weak, low frequency shoulder on the s_b lineshape (marked by a vertical dotted line). The inset shows the normalized (k_0 is the free space wave vector of the incident light) propagation constants of the coupled SPP modes, deduced from the Fourier spectra and plotted as a function of the film thickness. The solid curves are calculated with the analytical dispersion relations.

Fig. 9. Snapshots of the longitudinal and transverse electric field moduli taken at different instants during the simulation for excitation with 10 fs (intensity width) pulses. The simulation is for a 20 nm thick Ag film with a 200 nm slit, and 45° incidence angle to the surface normal.

Fig. 10. The position of the peak H_z field at the lower interface of the film as a function of the simulation time (left column), and the H_z field peak value as a function of its position (right column). (a) and (b) are for the s_b, (c) and (d) are for the a_b WPs. The results in (b) are obtained with a separate simulation performed on a horizontal scale of 60 μm.
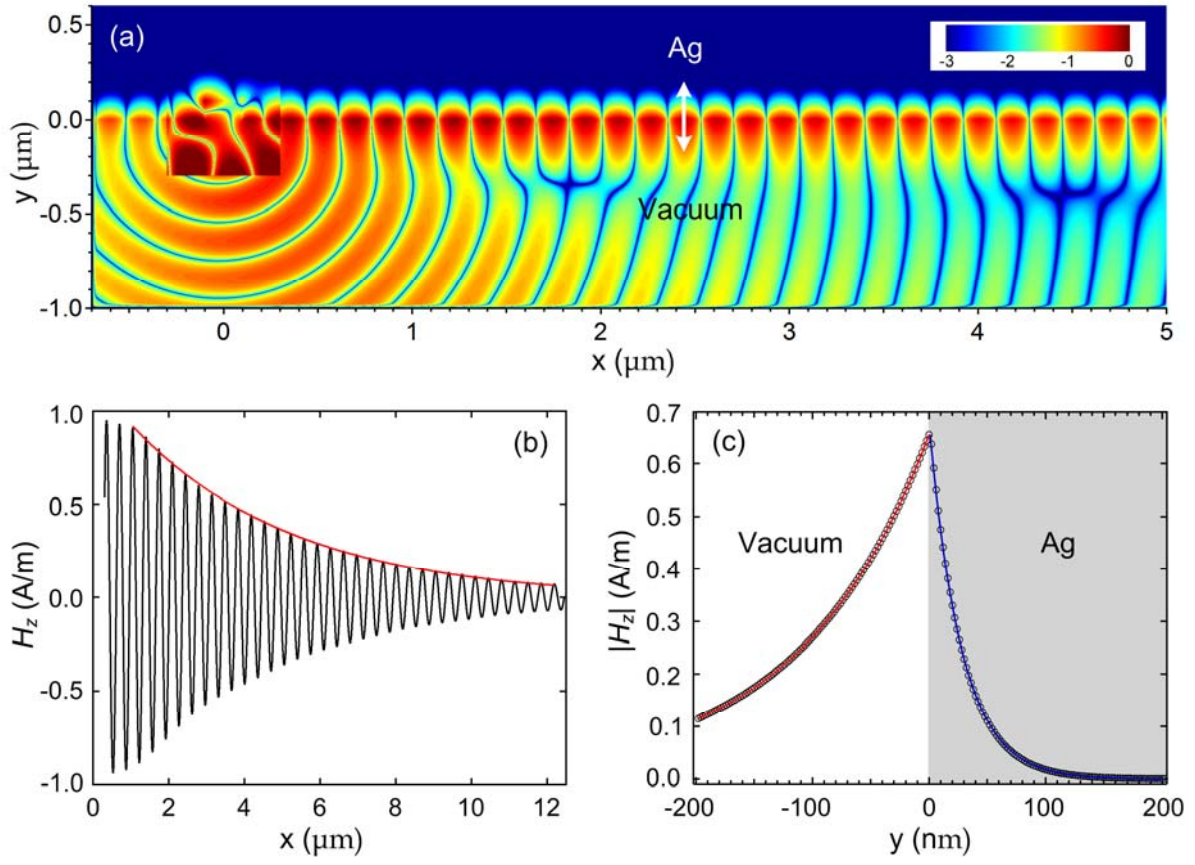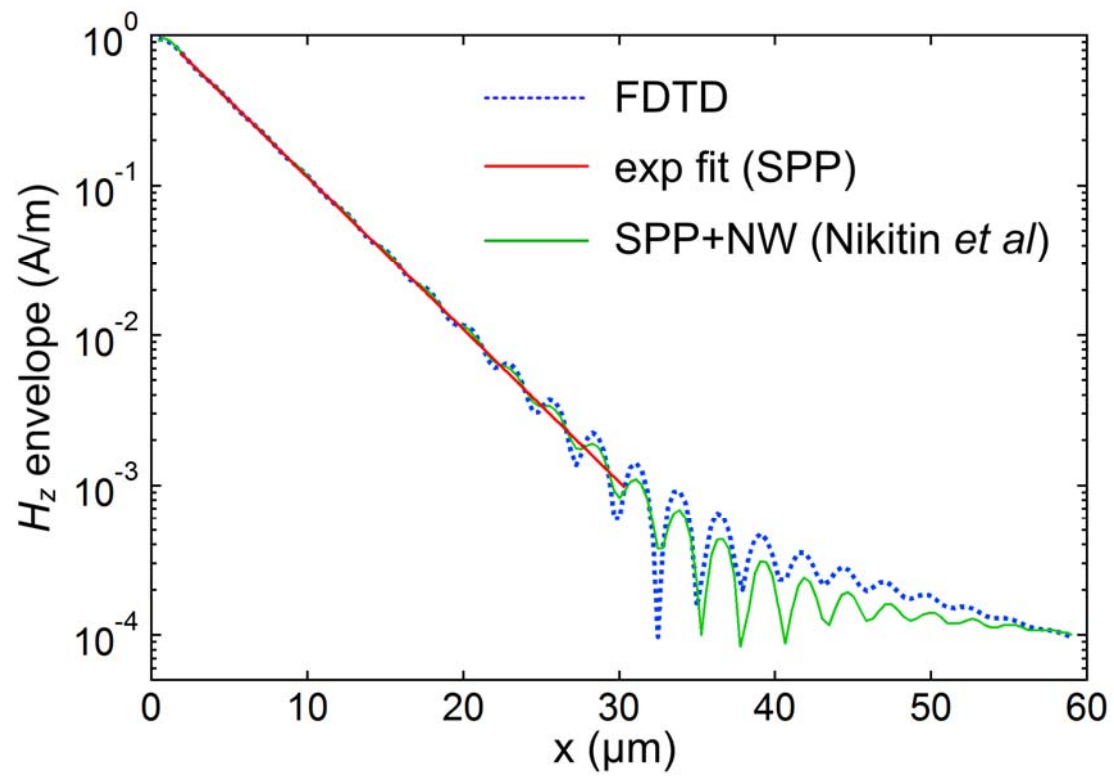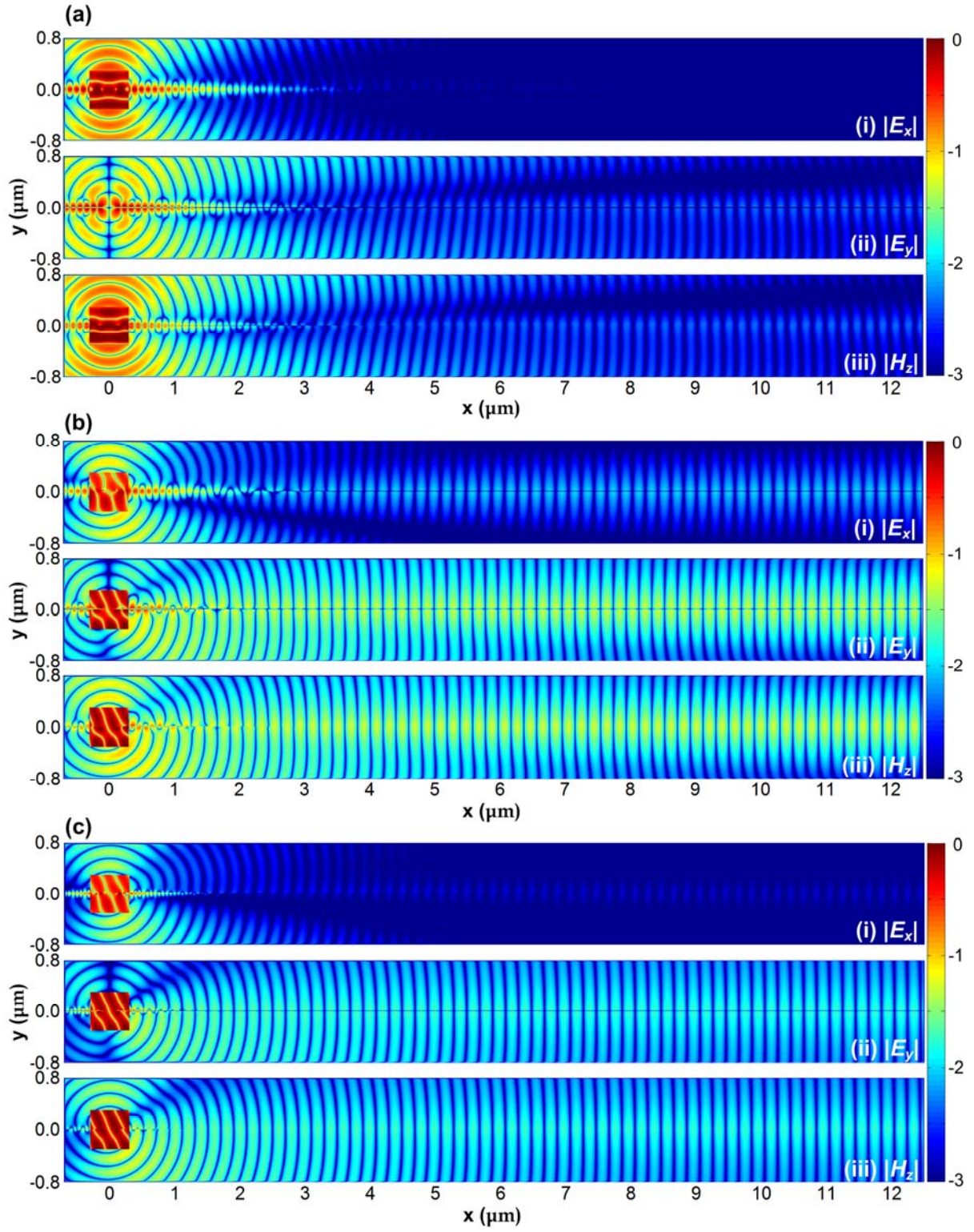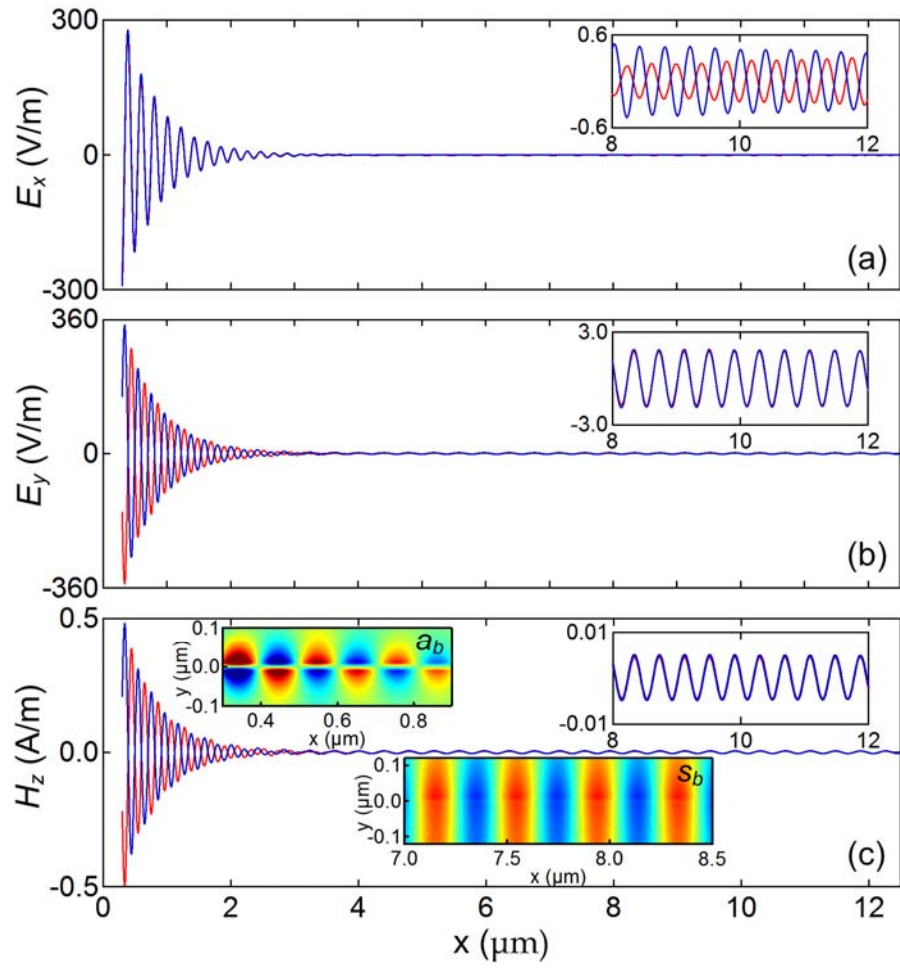
Fig. 1

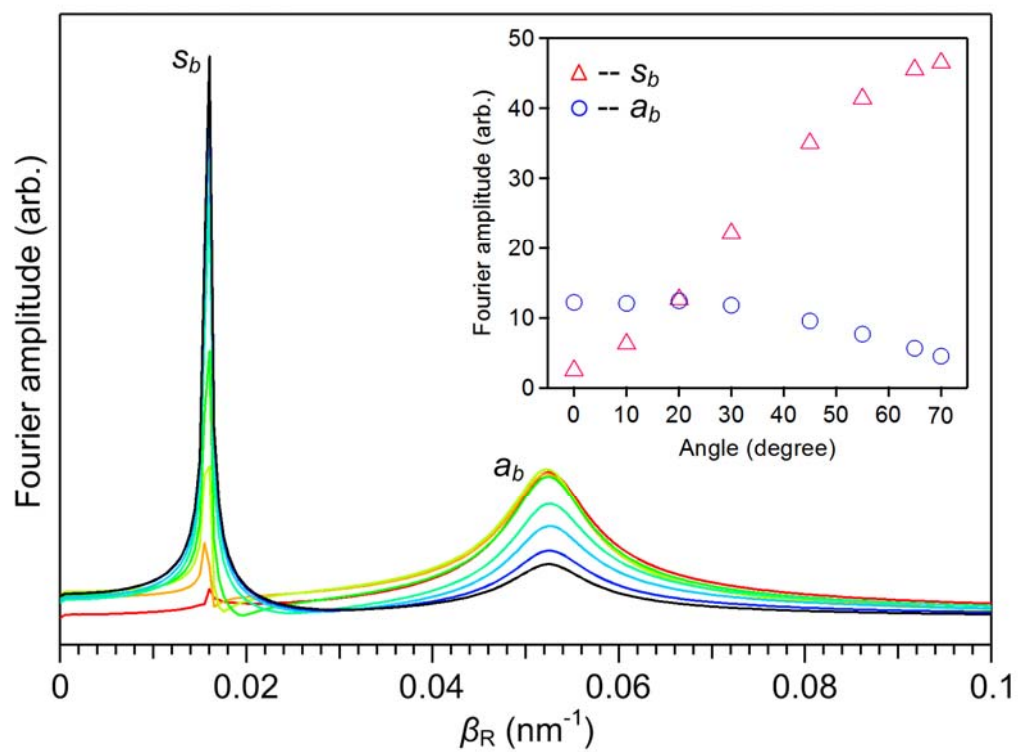Fig. 2

Fig.3

Fig. 4

Fig. 5

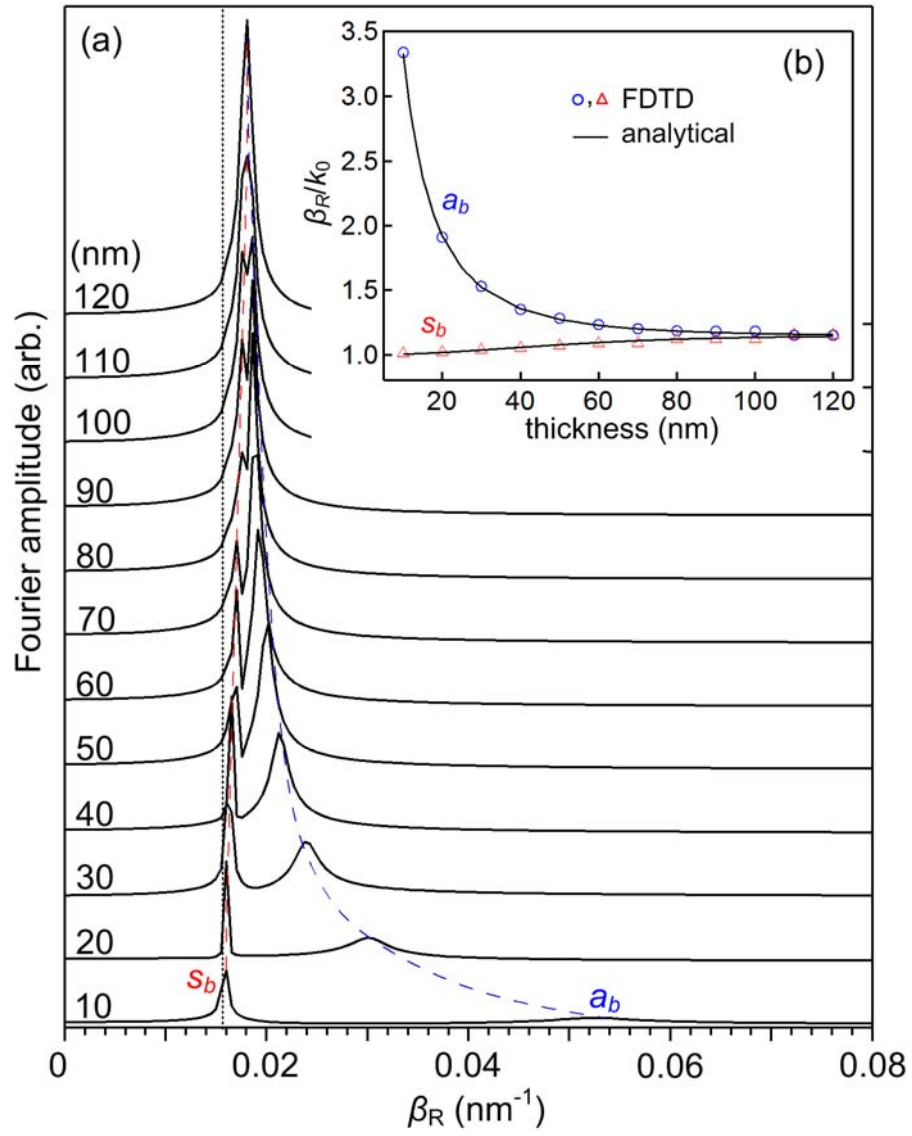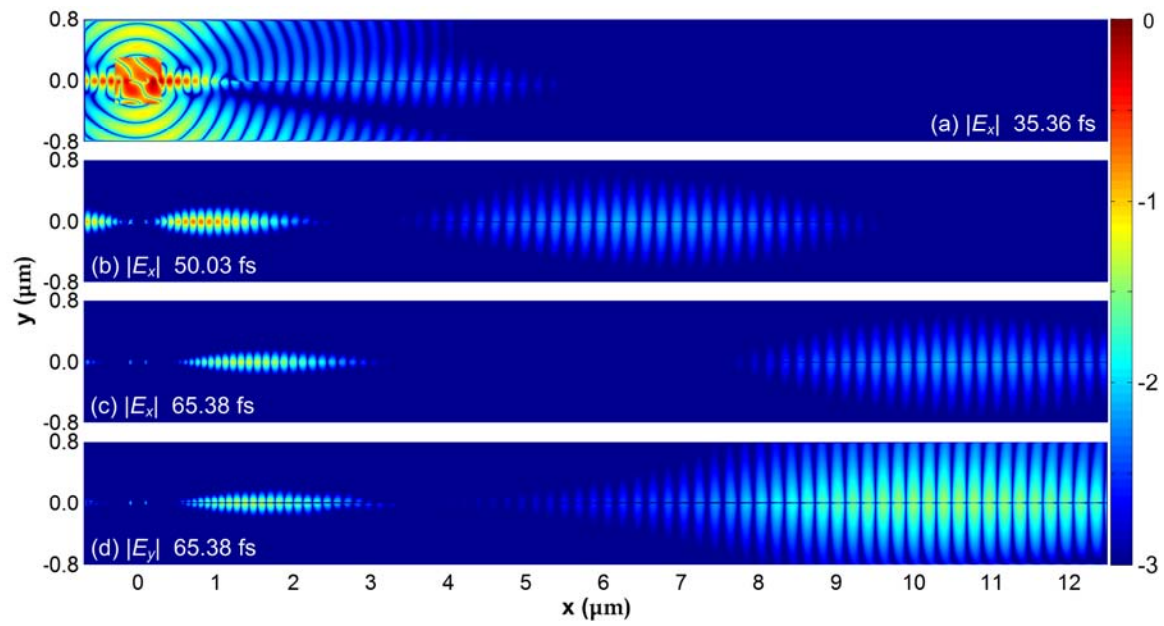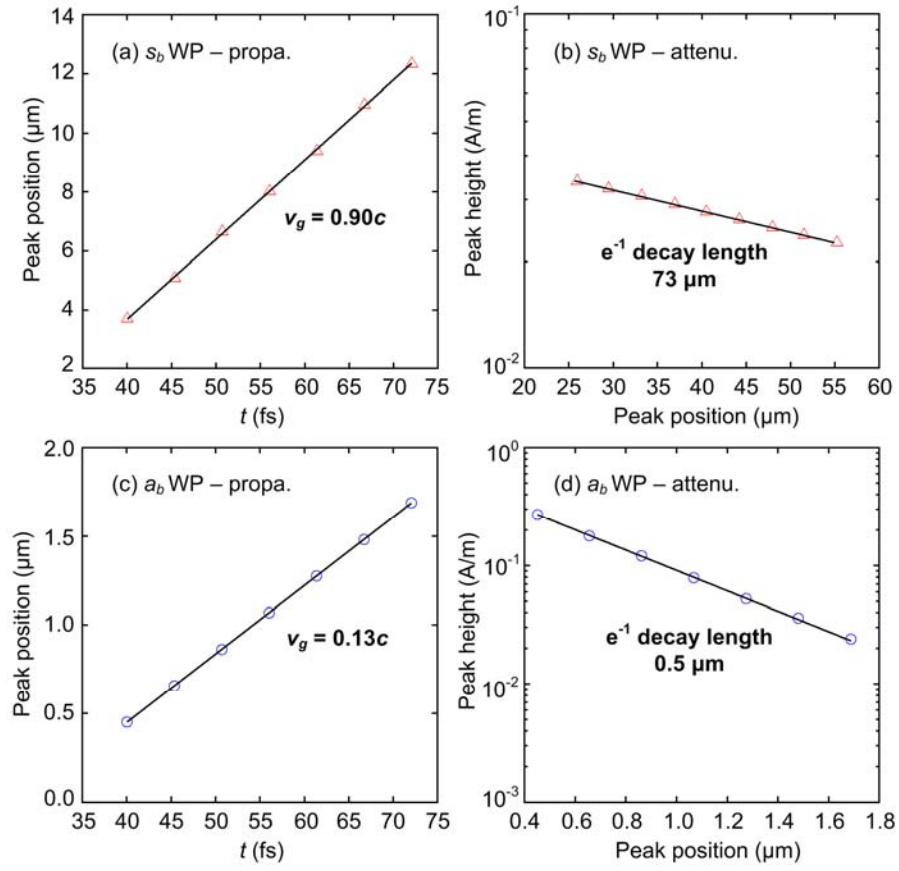Fig. 6

Fig. 7

Fig. 8

Fig. 9

Fig.10

References

[1]   H. Raether, *Surface Plasmons on Smooth and Rough Surfaces and on Gratings* (Springer, 1988).

[2]   S. A. Maier, *Plasmonics: Fundamentals and Applications* (Springer, New York, 2007).

[3]   K. A. Willets and R. P. Van Duyne, Annu. Rev. Phys. Chem. **58**, 267 (2007).

[4]   J. N. Anker, W. P. Hall, O. Lyandres, N. C. Shah, J. Zhao, and R. P. Van Duyne, Nat. Mater. **7**, 442 (2008).

[5]   W. L. Barnes, A. Dereux, and T. W. Ebbesen, Nature **424**, 824 (2003).

[6]   M. I. Stockman, New J. Phys. **10**, 025031 (2008).

[7]   T. Feurer, J. C. Vaughan, and K. A. Nelson, Science **299**, 374 (2003).

[8]   L. -X. Zhang, A. Kubo, L. -M. Wang, H. Petek, and T. Seideman, Phys. Rev. B **84**, 245442 (2011).

[9]   A. Otto, Z. Phys. **216**, 398 (1968).

[10] Y.-Y. Teng and E. A. Stern, Phys. Rev. Lett. **19**, 511 (1967).

[11] J. Renger, R. Quidant, N. van Hulst, S. Palomba, and L. Novotny, Phys. Rev. Lett. **103**, 266802 (2009).

[12] A. Kubo, N. Pontius, and H. Petek, Nano Lett. **7**, 470 (2007).

[13] C. Sönnichsen, A. C. Duch, G. Steininger, M. Koch, G. von Plessen, and J. Feldmann, Appl. Phys. Lett. **76**, 140 (2000).

[14] E. Devaux, T. W. Ebbesen, J.-C. Weeber, and A. Dereux, Appl. Phys. Lett. **83**, 4936 (2003).

[15] P. Berini, Adv. Opt. Photon. **1**, 484 (2009).

[16] J. J. Burke, G. I. Stegeman, and T. Tamir, Phys. Rev. B **33**, 5186 (1986).

[17] D. Sarid, Phys. Rev. Lett. **47**, 1927 (1981).

[18] R. Charbonneau, P. Berini, E. Berolo, and E. Lisicka-Shrzek, Opt. Lett. **25**, 844 (2000).

[19] A. E. Craig, G. A. Olson, and D. Sarid, Opt. Lett. **8**, 380 (1983).

[20] J. C. Quail, J. G. Rako, and H. J. Simon, Opt. Lett. **8**, 377 (1983).

[21] M. I. Stockman, Phys. Rev. Lett. **93**, 137404 (2004).

[22] S. Berweger, J. M. Atkin, X. G. Xu, R. L. Olmon, and M. B. Raschke, Nano Lett. **11**, 4309 (2011).

[23] E. N. Economou, Phys. Rev. **182**, 539 (1969).

[24] G. I. Stegeman, J. J. Burke, and D. G. Hall, Opt. Lett. **8**, 383 (1983).

[25] M. N. Zervas, Opt. Lett. **16**, 720 (1991).

[26] P. Berini and R. Buckley, J. Comput. Theor. Nanos. **6**, 2040 (2009).

[27] B. Yun, G. Hu, and Y. Cui, Opt. Express **17**, 3610 (2009).

[28] F. A. Burton and S. A. Cassidy, J. Lightwave Technol. **8**, 1843 (1990).

[29] G. Colas des Francs, J.-P. Hugonin, and J. Čtyroký, Opt. Quant. Electron. **42**, 557 (2011).

[30] T. J. Davis, Opt. Commun. **282**, 135 (2009).

[31] A. Degiron and D. Smith, Opt. Express **14**, 1611 (2006).

[32] G. Veronis and S. Fan, Opt. Lett. **30**, 3359 (2005).

[33] R. Zia, M. D. Selker, and M. L. Brongersma, Phys. Rev. B **71**, 165431 (2005).

[34] R. Müller and J. Bethge, Phys. Rev. B **82**, 115408 (2010).

[35] R. Müller, V. Malyarchuk, and C. Lienau, Phys. Rev. B **68**, 205415 (2003).

[36] A. Kubo, Y. S. Jung, H. K. Kim, and H. Petek, J. Phys. B: At. Mol. Opt. Phys. **40**, S259 (2007).

[37] K. F. MacDonald, Z. L. Samson, M. I. Stockman, and N. I. Zheludev, Nat. Photon. **3**, 55 (2009).

[38] A. Taflove and S. C. Hagness, *Computational Electrodynamcis: The Finite-Difference Time-Domain Method* (Artech House, Boston, 2005).

[39] F. López-Tejeira, F. J. García-Vidal, and L. Martín-Moreno, Phys. Rev. B **72**, 161405 (2005).

[40] V. Anikeyev, V. Temnov, U. Woggon, E. Devaux, and T. Ebbesen, Appl. Phys. B-Lasers O. **93**, 171 (2008).

[41]   G. Gay, O. Alloschery, B. Viaris de Lesegno, C. O'Dwyer, J. Weiner, and H. J. Lezec, Nat. Phys. **2**, 262 (2006).

[42]   P. Lalanne and J. P. Hugonin, Nat. Phys. **2**, 551 (2006).

[43]   P. Lalanne, J. P. Hugonin, H. T. Liu, and B. Wang, Surf. Sci. Rep. **64**, 453 (2009).

[44]   A. Y. Nikitin, S. G. Rodrigo, F. J. García-Vidal, and L. Martín-Moreno, New J. Phys. **11**, 123020 (2009).

[45]   F. J. Garcia-Vidal, S. G. Rodrigo, and L. Martín-Moreno, Nat. Phys. **2**, 790 (2006).

[46]   J. Weiner and H. J. Lezec, Nat. Phys. **2**, 791 (2006).

[47]   P. Lalanne, J. P. Hugonin, M. Besbes, and P. Bienstman, Nat. Phys. **2**, 792 (2006).

[48]   L. -X. Zhang, A. Kubo, L.-M. Wang, H. Petek, and T. Seideman, In preparation.

[49]   L. -X. Zhang and T. Seideman, Phys. Rev. B **82**, 155117 (2010).

[50]   I. R. Capoglu and G. S. Smith, IEEE Trans. Antennas. Propag. **56**, 158 (2008).

[51]   Y. N. Jiang, D. B. Ge, and S. J. Ding, Prog. Electromagn. Res. **83**, 157 (2008).

[52]   S. C. Winton, P. Kosmas, and C. M. Rappaport, IEEE Trans. Antennas. Propag. **53**, 1721 (2005).

[53]   J.-P. Bérenger, *Perfectly Matched Layer (PML) for Computational Electromagnetics* (Morgan & Claypool Publishers, 2007).

[54]   J. A. Roden and S. D. Gedney, Microw. Opt. Techn. Let. **27**, 334 (2000).

[55]   P. B. Johnson and R. W. Christy, Phys. Rev. B **6**, 4370 (1972).

[56]   A. Kawabat and R. Kubo, J. Phys. Soc. Jpn. **21**, 1765 (1966).

[57]   D. F. Zaretsky, P. A. Korneev, S. V. Popruzhenko, and W. Becker, J. Phys. B: At. Mol. Opt. Phys. **37**, 4817 (2004).

[58]   A. Kubo, K. Onda, H. Petek, Z. Sun, Y. S. Jung, and H. K. Kim, Nano Lett. **5**, 1123 (2005).

[59]   The wavelengths of SPP and QCW can be estimated by directly measuring the periodicity of the surface wave (dominated by SPP) and the radiating wave (dominated by the far-field component of the QCW) in Fig. 2(a). Alternatively, they can be deduced from the Fourier transform of the Hz field profile along the interface in the range of, e.g. $30 - 45$ μm, where the SPP and QCW bear comparable Fourier amplitudes (see Fig. 3).

[60]   H. W. Kihm, J. H. Kang, J. S. Kyoung, K. G. Lee, M. A. Seo, and K. J. Ahn, Appl. Phys. Lett. **94**, 141102 (2009).

[61]   See supplemental material at[ ]for the movie showing the temporal evolution of the Hz field profile and its corronsponding Fourier spectrum at an Ag-vacuum interface upon the excitation by a ~10 fs 400nm pulse at 65° incidence.

[62]   J. M. Pitarke, V. M. Silkin, E. V. Chulkov, and P. M. Echenique, Rep. Prog. Phys. **70**, 1 (2007).

[63]   See supplemental material at[ ]for the movies showing the evolution of the Ex, Ey, and Hz field distrubuitions in a 20 nm thick Ag film upon the excitation by a ~10 fs 400nm pulse at 45° incidence.